ORIGINAL RESEARCH ARTICLE

Processing and characterization of crack-free 7075 aluminum alloys with elemental Zr modification by laser powder bed fusion

Wenhui Yu[1,2], Zhen Xiao[1,3,4]*, Xuhui Zhang[1], Yetao Sun[1], Peng Xue[2], Shuai Tan[2], Yongling Wu[1], Hongyu Zheng[1]*

[1]School of Mechanical Engineering, Shandong University of Technology, 255000, Zibo, Shandong, P.R. China

[2]Shengli Oilfield highland Petroleum Equipment Co., Ltd, 257091, Dongying, Shandong, P.R. China

[3]School of Transportation and Vehicle Engineering, Shandong University of Technology, 255000, Zibo, Shandong, P.R. China

[4]PrinxChengshan (Shandong) Tire Co., Ltd, 264300, Weihai, Shandong, P.R. China

*Corresponding authors:
Zhen Xiao
(xiaozhen@sdut.edu.cn);
Hongyu Zheng
(zhenghongyu@sdut.edu.cn)

Abstract

High-performance engineering alloys, such as 7000 series aluminum alloys, suffer poor printability in laser powder bed fusion (LPBF) additive manufacturing. An enormous challenge lies in the suppression of solidification cracks caused by solidification shrinkage and thermal stresses. Porosity formation, as one of the main concerns for LPBF application, should also be avoided at the same time. In this study, aluminum alloy (AA) 7075 with and without Zr modification was additively manufactured by LPBF. Processing parameters of laser power and scanning speed, resulting in various volumetric energy density (VED), were experimentally determined to produce crack-free components with tailored microstructure. Optical microscopy was used to reveal how the crack density and porosity vary with VED. Scanning electron microscopy and transmission electron microscopy uncovered the detailed microstructure in the molten pool and the evolution of the elemental Zr addition. The results indicate that 1 w.t.% addition of elemental Zr in AA7075 led to lower crack density compared with 0.3 w.t.% addition. In 1 w.t.% Zr-modified AA7075, crack-free components were obtained under high VED. Fine equiaxed grains, instead of large columnar grains, were formed at the bottom of the molten pool boundary due to the existence of Al_3Zr compound, which favored the nucleation of aluminum grains and elimination of cracks. The phenomenon of silicon segregation near cracks remained in Zr modified alloys, although its effects on cracking were suppressed. Spherical pores in the Zr-modified AA7075 increased due to the deterioration of fluidity by unmelted particles, which distracted the Marangoni flow as well. Sufficient laser energy input can increase the viscosity and ease the pores escaping. By optimizing parameters, crack-free AA7075 parts with low porosity can be manufactured through LPBF with Zr addition.

Keywords: Laser powder bed fusion; 7075 aluminum alloys; Zr modification; Crack elimination; Porosity

1. Introduction

Laser powder bed fusion (LPBF), as an important laser-based additive manufacturing (AM) technique for metal components, is considered one of the most innovative technologies in Industry 4.0[1-4]. It provides an opportunity to manufacture components with complex geometries in the aerospace, automotive, and medical industries[5,6]. LPBF enables successive layer assembly with a laser beam as the heat source. The localized heat input in micron length and time scale induces rapid melting and consolidation through the formation of a molten metal pool[7,8]. The numerous thermal cycles during processing thereby lead to unique microstructural features, which are in favor of high mechanical strength. However, there are several concerns for the widespread application of the LPBF technique, among which defects are important obstacles. Porosity and cracks, as the most common defects, have been investigated for decades to reveal the mechanisms of defect formation and migration methodology[9,10].

Porosity formation in LPBF largely depends on the thermal history of the molten pool[11,12]. Lack of fusion defects are easily formed if the thermal input is too low to fuse the powder to the substrate or the underlying layer. Conversely, if the thermal input is too high, the molten metal evaporates vigorously, and the intense vapor recoil pressure will suppress the melt surface, creating large keyhole-induced porosity at the bottom of the molten pool. Even when the thermal input is intermediate, there are possibilities for the formation of metallurgical pores, originated from entrapped gases, such as shielding gas, vapor, hydrogen, and gases entrapped during powder atomization process. These are usually small spherical pores that are driven by Marangoni flow and fail to escape from the molten pools. Migration of porosity relies on optimizing the processing parameters. Tang et al.[13] proposed a prediction model for lack of fusion porosity with the fundamental parameters, including melt-pool cross-sectional dimensions, hatch spacing and layer thickness, and investigated their influence on the defect. Plessis et al.[14] elaborated how different processing parameters result in different pores formation mechanisms. The three-dimensional morphologies of lack of fusion porosity, metallurgical pore, and keyhole mode pore have been revealed as irregular, near-spherical, and rounded, but not spherical. Leung et al.[15] uncovered mechanisms of pore migration by Marangoni-driven flow, pore dissolution, and dispersion by laser re-melting through in situ and operando high-speed synchrotron X-ray imaging. Marangoni-driven flow causes the melt with a high surface tension to fold over the surface of the melting track and entrain an argon bubble, and allows the pores inside the molten pool to escape as well. Laser re-melting between layers promotes existing pores in the previous layer to coalesce and grow at the expense of others. They also found that the subsequent laser re-melting caused by the next cycles helps to disperse large pores into smaller ones, rather than eliminating them due to the relationship of gas solubility and temperature. However, the whole re-melting of laser tracks helps to degas the melt track because it allows the entrapped gas at the bottom of the molten pool to float up and escape[16].

Cracking is another typical defect in LPBF-manufactured parts[17,18]. Solidification cracking is the most common in LPBF and is mainly related to the materials compositions[19,20] although elaborate control of processing may only work to some extent[21]. It occurs in the mushy zone of an alloy at the final stage of solidification. At this stage, the liquid films between adjacent dendrites can be easily torn due to the solidification shrinkage and thermal stresses upon cooling. In addition, adjacent arms coalesce and form a solid skeleton, resulting in poor liquid feeding[22]. Cavity forms in the weak intergranular regions and propagate through interdendritic colonies and even layers. Therefore, most conventional alloys cannot be readily additively manufactured. Appropriate alloys must be carefully selected or modified so as to increase the printability of LPBF. High-strength 7xxx series aluminum alloys (AA) are typical types that are unfriendly to the LPBF process due to their high laser reflectivity, easy reactivity with oxygen, and especially, crack sensitivity[23,24]. Crack elimination is of the first priority for the qualified performance of the LPBF-manufactured high strength AA parts. Recently, a growing number of researchers began focusing on this topic[25-29]. Otani et al.[30] found that silicon additions into AA7075 help to yield better process ability by suppressing the voids and cracking. However, high silicon content would induce a tradeoff between strength and ductility and must be carefully adjusted. Modification with transition elements, such as Sc and/or Zr, has shed new light on achieving crack-free aluminum components by LPBF. These elements offer the possibilities for a strong grain refinement due to the precipitation of coherent $L1_2$ structured Al_3Sc, Al_3Zr, and $Al_3(Sc,Zr)$ and have proven to be effective in crack reduction through equiaxed microstructure in recent works[31]. Pre-alloyed Sc- and Zr- modified AA were found to enable high proportion of fine equiaxed grains and therefore lead to high mechanical strength[32-34]. However, the application of Sc has been limited due to the inherent corrosion sensitivity and laser incompatibility issues[35]. Zr, a less expensive alternative, has therefore found more applications in the refinement of grains in both traditional and LPBF processing. Er has attracted a growing interest as a modification element for the high-strength AA manufactured through LPBF[36].

However, crack density decreased at the expense of relative density as porosity became an issue with additives. Therefore, crack-free and pore-free fabrication of AA7075 is a very difficult task. Many researchers have placed their focus on either porosity or cracking. Therefore, it is imperative to devise a method to fabricate crack-free samples with low porosity.

The present study aims to find the process window for the production of crack-free components of the Zr modified high-strength AA7075 alloy with low porosity. It is known that the maximum solid solubility of Zr in Al is ~ 0.25 w.t.% under equilibrium solidification conditions[37]. However, LPBF processing involves rapid heating and cooling cycles under far-from-equilibrium conditions, which may significantly enhance Zr solubility. Taking consideration the melting conditions of elemental powders as well, the concentrations of 0.3 w.t.% and 1 w.t.% Zr were investigated to find out whether a suitable amount of Zr is able to achieve sufficient precipitation of Al-Zr intermetallic nucleants. The relationship between the processing parameters and defects features was further investigated in the modified AA7075. The results of this study would contribute to a better understanding of defect formation in Zr-modified AA7075 through LPBF.

2. Materials and methods

The materials prepared for the LPBF fabrication were commercial spherical AA7075 powders and irregular Zr particles (supplied by Beijing Crigoo Materials Technology Co., Ltd.). The size of the AA7075 powders ranges between 20 and 63 μm while elemental Zr powders were sieved to remove particles with a size over 75 μm. The chemical composition analysis of the as-received AA7075 and Zr powders was performed using inductively coupled plasma optical emission spectroscopy (ICP-OES, NCS Plasma 3000). The chemical compositions of the as-received AA7075 and Zr powders are listed in Table 1. They were blended to prepare modified AA7075 alloys with different contents, 0.3 w.t.% and 1 w.t.%, respectively. The mixtures were ball milled in an argon atmosphere for 16 h at a rotation rate of 300 rpm. The ball-to-powder weight ratio was 1:1. ZrO_2 milling balls, consisted of 20% of them having a diameter of 15 mm, 50% having a diameter of 12 mm and 30% having a diameter of 5 mm, were employed in a corundum jar. Figure 1 displays the morphology of the AA7075, elemental Zr, and blended powders. Figure 1E-H show the close-up view of the respective powders, indicating that the ball milling process maintains the original surface morphology and shape of the AA7075 powders. The green arrows in Figure 1C and D mark the irregular Zr particles. As expected, more irregular particles can be found in powders with 1 w.t.% additives. In Figure 1I, the bright white areas indicated by the green arrows in the back-scattered electron image refer to Zr. As seen, Zr particles with size around 1 μm adhered to the aluminum powders. Moreover, elemental particles with size larger than 20 μm were rarely found as the original particles had cracks and could be milled into smaller ones.

Parts with a 5 × 5 × 6 mm dimension were fabricated on a substrate using an SLM 125 HL machine (SLM Solutions Group AG, Lubeck, Germany), which is equipped with a fiber laser (1064 nm), with a maximum laser power of 400 W and a focus diameter of 80 μm. An argon atmosphere with <0.1% oxygen was provided to prevent oxidation and interstitial element contaminations during the manufacturing process. To decrease the thermal stress, the substrate was preheated to 150°C before fabrication. Sixty-four samples classified in 16 groups were printed in order to obtain the processing window. The laser power ranges from 250 to 325 W, with an interval of 25 W, and the scanning speed ranges from 1000 to 1300 mm/s, with an interval of 100 mm/s. Table 2 lists the volumetric energy density (*VED*) which can be calculated by **Equation 1**.

$$VED = P/vht \tag{1}$$

where P is the laser power (W), v is the scanning speed (mm/s), h is the hatching space (μm), and t is the layer thickness (μm). The hatching space and layer thickness in the present study were 120 μm and 30 μm, respectively. Figure 2 shows how the 64 parts were fabricated with the scanning strategy. The planes for further characterization are also illustrated in the upper right inset.

After fabrication, the samples were removed from the substrate via wire-cut electrical discharge machining (EDM). The parts were then cleaned by sonicating in ethanol and dried with clean compressed dry air. Density

Table 1. Chemical compositions of the AA7075 and Zr powders in w.t. %.

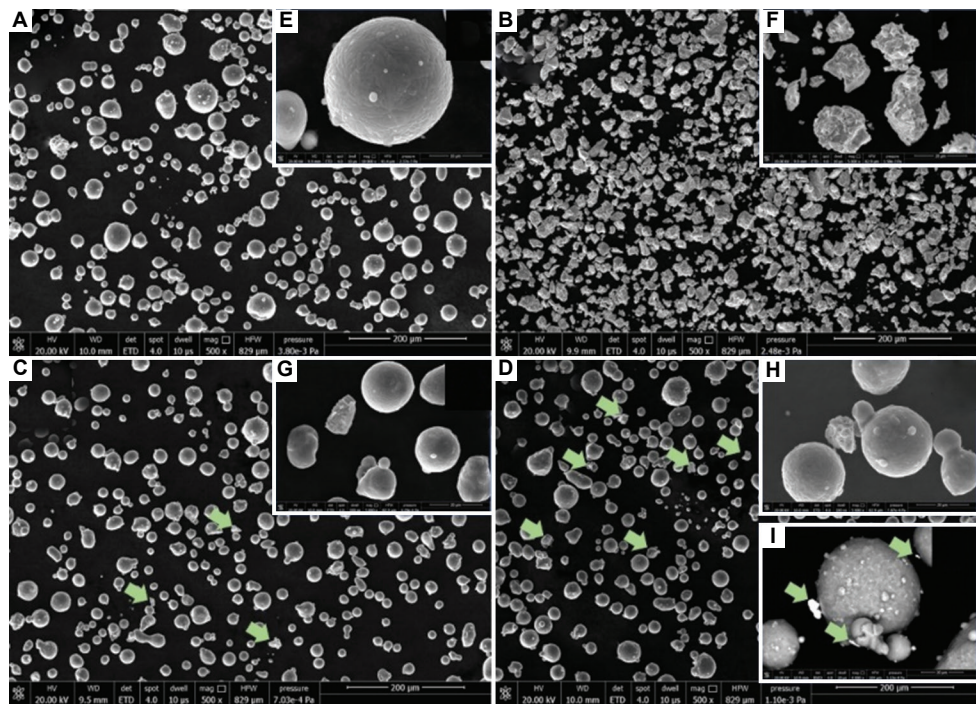| Elements	Si	Fe	Mg	Cr	Zn	Cu	Mn	Ti	Ca	Cr	H	O	Zr	Al
Alloys														
AA7075	0.06	0.06	2.53	0.21	5.9	1.57	<0.02	0.005	/	/	/	0.046	/	Bal.
Zr	0.001	0.098	0.001	0.012	/	/	/	/	0.003	0.012	0.002	0.094	Bal.	0.001

Figure 1. SEM images of (A) as-received AA7075 powders, (B) Zr particles, (C) 0.3 w.t.% Zr-modified AA7075 powders, and (D) 1 w.t.% Zr-modified AA7075 powders. The green arrows indicate the irregular particles. (Insets E–H) Detailed morphologies of the powders, respectively, (Inset I) back-scattered electron image.

Table 2. Volumetric energy density (*VED*, J/mm³) over various laser power and scanning speed.

Laser power (W)	250	275	300	325
Scanning speed (mm/s)				
1000	69	76	83	90
1100	63	69	76	82
1200	58	64	69	75
1300	53	58	64	69

measurements were taken based on Archimedes' principle. The microstructural blocks were mounted in epoxy resin and subjected to grinding and polishing. Grinding was done with 400, 600, 800, and 1000 grit sandpapers. Polishing was carried out using 2.5 μm and 0.5 μm diamond. To calculate the crack density and porosity, the mounted samples were observed with an optical microscope (OM; Olympus BX53M, Olympus Corporation, Japan). The crack density and porosity measurement procedures based on these OM images without etching are formulated as **Equations 2** and **3**.

$$Crack\,density, C\,(/um) = \frac{\sum_{n=1}^{i} l_i}{A} \times 100\%$$

(2)

where l_i represents the length of a single crack (μm), A represents the total area of the OM images.

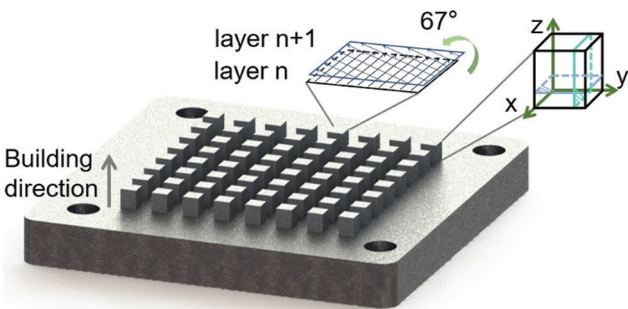**Figure 2.** Fabricated samples on the substrate and the scanning strategies. The xz and xy planes in the inset are used for observing defects.

$$Porosity, P\,(\%) = \frac{\sum_{n=1}^{i} A_i}{A} \times 100\%$$

(3)

where A_i represents the area of a single pore (μm²). It should be noted that the crack density and porosity were calculated based on two-dimensional images, which might be different from the overall data. However, the results are believed to be reliable in reflecting the major characteristics.

Some samples were etched for 8 s with Keller's reagent to reveal the microstructure in the molten pool. These blocks were characterized with an OM and with a scanning electron microscope (SEM; Quanta 250, FEI Company,
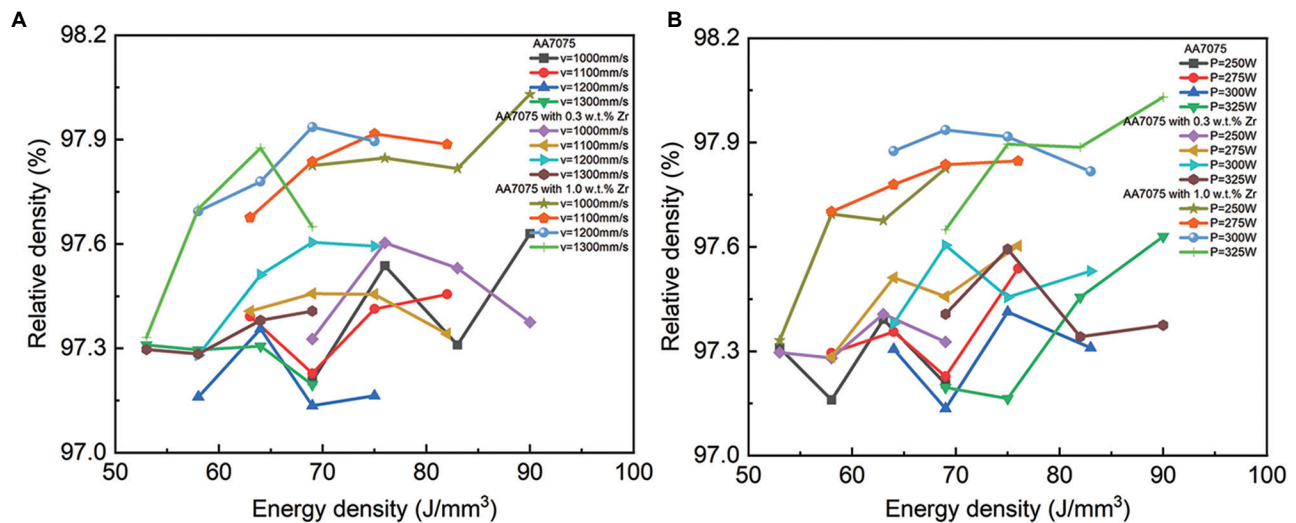
Figure 3. Relative density of the LPBF AA7075 of different chemical compositions under various (A) laser power and (B) scanning speed.

Hillsboro, OR, USA) for detailed microstructure. Transmission electron microscope (TEM) and scanning TEM (STEM) were performed at 200 kV using a Tecnai G2 Spirit TWIN equipped with an energy dispersive X-ray spectrometer (EDS) to evaluate microstructure evolution, particularly the distribution of elemental Zr. The TEM sample was prepared by grinding and polishing a small piece of the printed block to about 100–120 μm thickness, and then cutting 3 mm disks using a disk punch. The disks were ion-beam thinned for microstructural observation.

3. Results and discussion

3.1. Relative density

Relative density, the ratio of the measured density of LPBF-fabricated parts to the theoretical density of bulk materials, is a reflection of both cracks and porosity. Figure 3 shows how the relative densities of alloys with different compositions vary with VED. Figure 3A and B display the influence of laser power and scanning speed, respectively. It can be seen that the density of AA7075 is sensitive to laser power over the low VED range. Parts printed using 0.3 w.t.% Zr-modified AA7075 resemble to their counterparts fabricated with as-received powders. The relative density of AA7075 with 1 w.t.% Zr addition has a positive relation with laser power over the full VED range. On the other hand, the density of AA7075 with low Zr addition is sensitive to scanning speed over the high VED range. More Zr addition leads to higher sensitivity to scanning speed. Different laser power and scanning speed may lead to the same VED; hence, the relative densities under the same VED were combined, as shown in Figure 4. The relative density of the AA7075 grew with
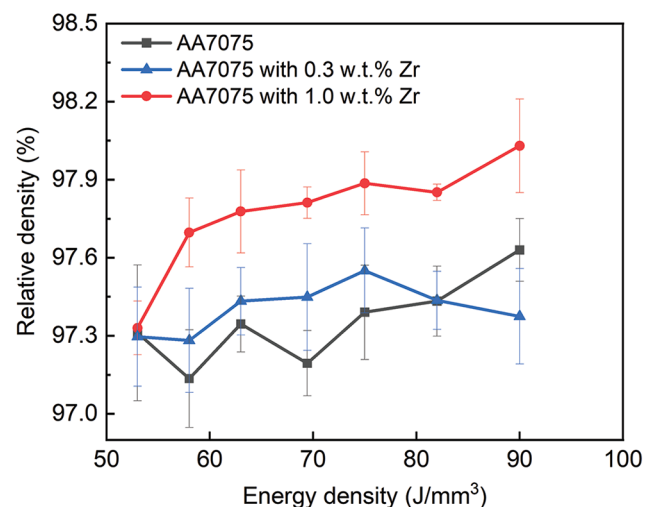

Figure 4. Relative density of the LPBF AA7075 of different chemical compositions under different VED.

the increase of the VED. The phenomenon is similar when Zr was mixed. It is also interesting to know that when the VED is as low as 53 J/mm³, the relative densities for the three alloys were close, which means that Zr additions show little effect. The relative density of the AA7075 with 1 w.t.% Zr addition turns out to be the highest over that of the AA7075 and 0.3 w.t.% Zr-modified alloys. 0.3 w.t.% Zr addition only contributed to a slight increment in relative density compared with that of the unmodified bulks.

3.2. Crack

Figure 5 shows the representative microstructure along the building direction of the three printed parts. The 0.3
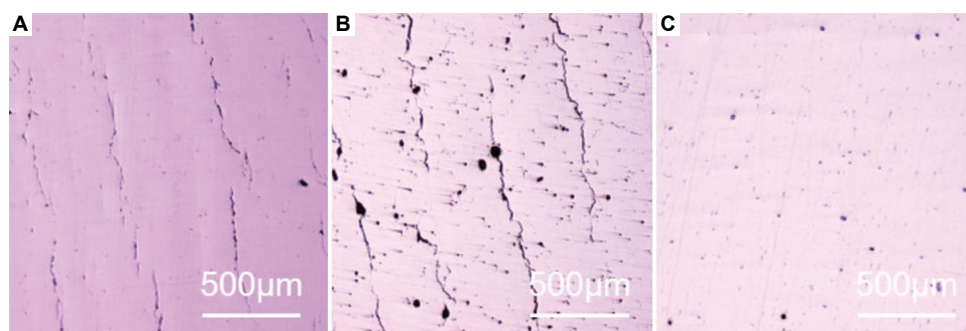
Figure 5. Representative microstructure of (A) as-received AA7075, (B) 0.3 w.t.% Zr-modified AA7075, and (C) 1 w.t.% Zr-modified AA7075.

w.t.% Zr-modified alloy exhibits long cracks propagating through layers, similar to that in the AA7075 alloys, while low crack density in 1 w.t.% Zr-modified alloy is achievable with the optimization of parameters. As described, the 0.3 w.t.% Zr-modified alloys show low relative density, which is verified by the optical images. This indicates that 0.3 w.t.% Zr is not sufficient for the modification. The comparison of the Zr distribution in Figure 1C and **D** may account for this phenomenon. With 1 w.t.% Zr addition, there were more particles being distributed around the AA powders and melted in the molten pool. Therefore, the crack density and porosity of 0.3 w.t.% Zr-modified alloy were not further characterized in this study.

Cracking is one of the main reasons that results in voids, particularly in LPBF 7075 alloy bulks. Crack density on both xz and xy planes was calculated and plotted, as shown in Figure 6. The crack density on xz plane of AA7075 ranges in $1.50 \times 10^{-3}/\mu m$ – $1.71 \times 10^{-3}/\mu m$ with minor fluctuation under various VED. With 1 w.t.% Zr addition, the corresponding crack density decreased to the range of $3.69 \times 10^{-4}/\mu m$ – $9.38 \times 10^{-4}/\mu m$. The cracks density leveled off with VED higher than 69 J/mm³. The crack density on xy plane was much higher than that on the xz plane. A large reduction in crack density was observed on the xy plane with Zr addition. A peak emerged at 69 J/mm³ VED. The crack density decreased to as low as $1.34 \times 10^{-3}/\mu m$ and $1.03 \times 10^{-3}/\mu m$ at 82 J/mm³ and 90 J/mm³, respectively.

3.3. Porosity

Porosity is another main factor for relative density. Figure 7 shows the calculated porosity based on OM images on the xz and xy planes. Overall, the Zr-modified AA7075 show higher porosity over the low VED range. When the VED goes up, the porosity decreases to even lower than that in AA7075. An obvious negative correlation between porosity on xy plane and VED was observed. This indicates that alloys with Zr addition require higher energy input.
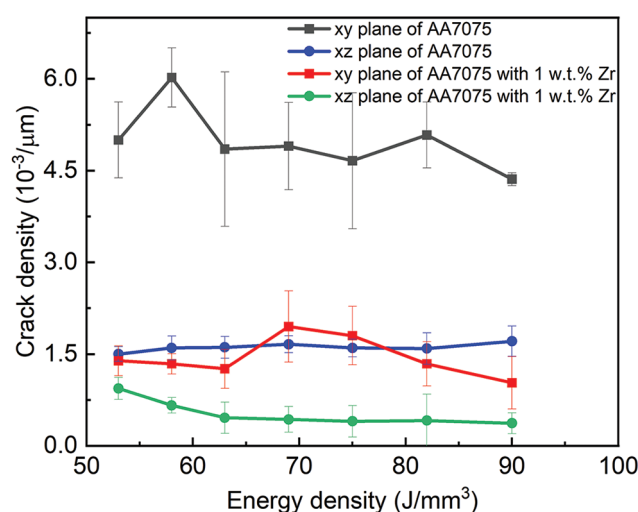

Figure 6. Crack density on xz and xy planes of the LPBF AA7075 and 1 w.t.% Zr-modified AA7075 under different VED.

When the VED is above 82 J/mm³, the samples display low porosity on both planes, confirming that we obtained crack-free components with low porosity.

3.4. Microstructure

A group of samples with scanning speed of 1100 mm/s and laser power ranging from 250 W to 325 W were further characterized to investigate the microstructural evolution. Their VED values – 63 J/mm³, 69 J/mm³, 76 J/mm³, and 82 J/mm³ – are shown in Table 2. Figure 8 shows the representative microstructure of these samples. The sample with VED at 63 J/mm³ exhibited coarse and long cracks propagating through numerous layers, as seen in Figure 8A. When the laser power increased from 250 W to 300 W, cracks propagating within shorter distance were observed. In Figure 8D, few cracks were observed, indicating that low crack density can be achieved with high laser energy input. Figure 8M-P show the detailed structures inside the molten pool. Large columnar grains
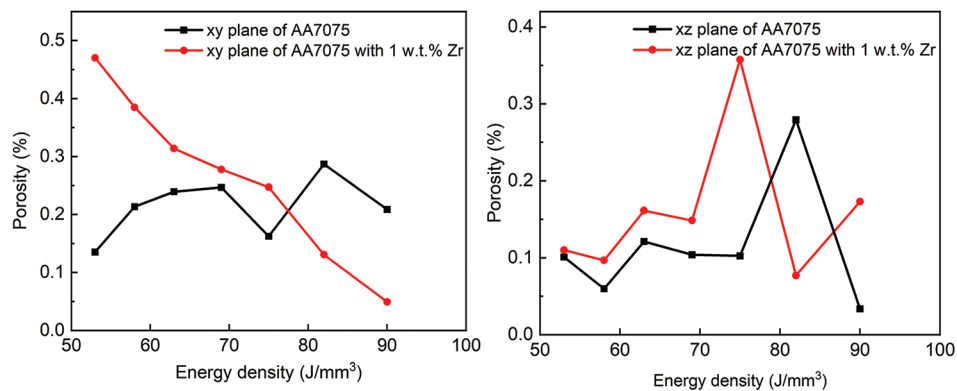
Figure 7. Porosity on xz and xy planes of the LPBF AA7075 and 1 w.t.% Zr-modified AA7075 under different VED.
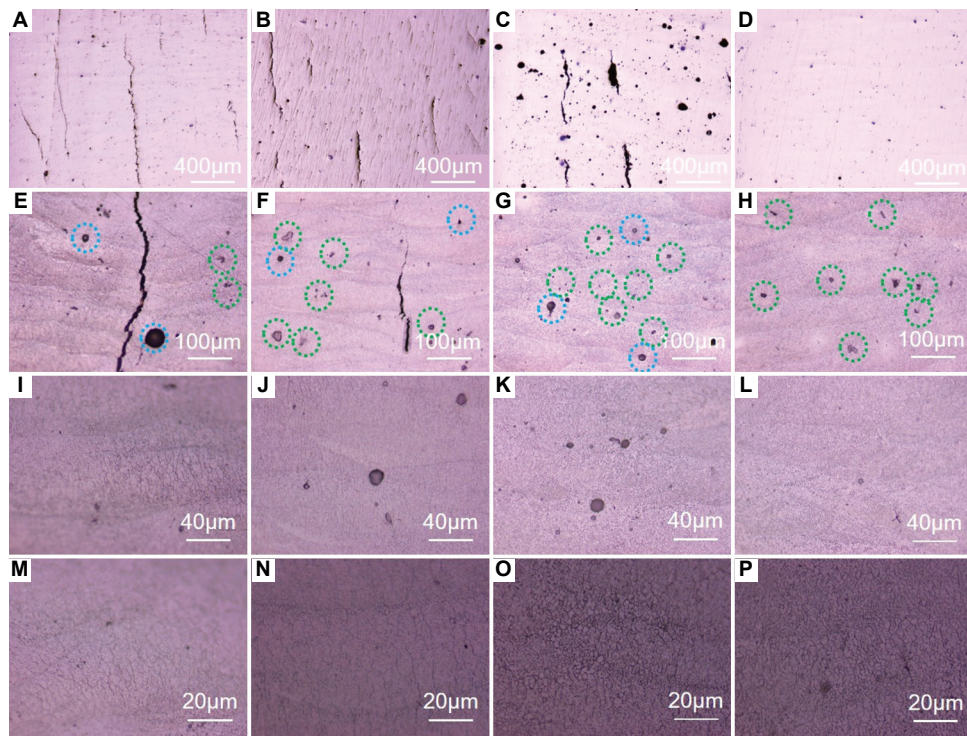

Figure 8. Representative microstructure of samples with scanning speed 1100 mm/s and laser power (A, E, I, M) 250 W, (B, F, J, N) 275 W, (C, G, K, O) 300 W, and (D, H, L, P) 325 W, respectively.

formed under low VED, as shown in Figure 8M and N. In the microstructure of samples with VED at 76 J/mm³, equiaxed grains began to emerge. When the laser energy input kept increasing, the proportion of equiaxed grains grew, which is the reason that the cracks are suppressed.

The blue circles in Figure 8 mark the pores, which are mainly in spherical shape. The particles marked by green circles are unmelted Zr particles, which could be mistaken for the pores in OM images. They can be distinguished in the SEM images. SEM images were taken on the samples with and without 1 w.t.% Zr addition, as shown

in Figure 9. The white particles marked by green circles in Figure 9B represent the Zr particles. It is worth noting that although numerous Zr particles remain unmelted, there is no evidence that the pores are connected to them. Undoubtedly, it is Zr addition that induces more spherical pores. As keyhole pores are asserted to be round but not spherical in a previous study[14], the emerged pores are believed to be entrapped gas[38]. The emergence of the pores can be attributed to deterioration of the melt viscosity, which prevents the escape of gases. In fact, the molten pool with low laser energy input is subjected to low viscosity

inherently. The existence of Zr particles exacerbates the poor fluidity and distract the Marangoni flow, resulting in more entrapped gas[36]. A similar phenomenon also occurred in metal matrix composites[39]. When more thermal energy is absorbed, the Marangoni flow grows stronger and allows more bubbles to escape[40].
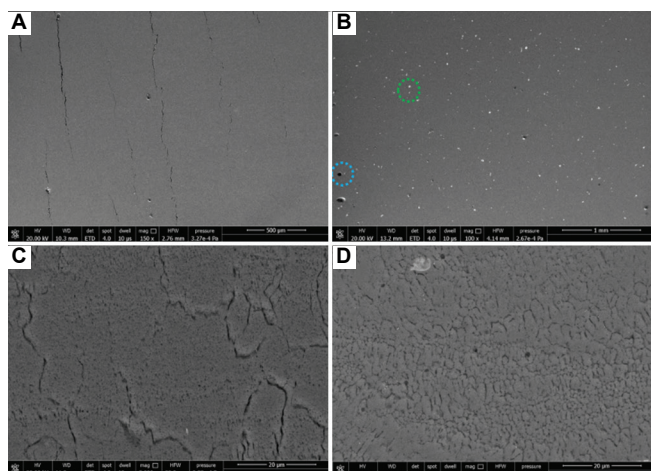
Figure 9C and D show how the grains were distributed in modified samples with VED at 64 and 82 J/mm³, respectively. Extremely fine equiaxed grains were observed in the sample with high VED, which is in agreement with the results shown in Figure 8M and P. To investigate the underlying mechanisms, a TEM analysis was carried out on the modified sample fabricated with VED at 82 J/mm³, as displayed in Figure 10. The particles inside the grains were analyzed with EDS in STEM mode, revealing the constituent elements. The particle at spot 1 is made up of Al, Zr and minor Zn, indicating the existence of the Al_3Zr compound. It is speculated that the elemental Zr melts and reacts to form the Al_3Zr compound, which exhibits <0.52% lattice mismatch with the primary face-centered-cubic aluminum phase and therefore provides an ideal low-energy heterogeneous nucleation site[17,41]. Therefore, the extremely fine equiaxed grains with size ranging from 1 to 4 μm formed, as shown in Figure 10**A**. Particles at spot 2 containing Al, Zn, Mg, Cu, and Si elements can be identified to be the secondary phases of the AA7075. It seems that some fine grains are devoid of the nuclei. They are supposed to be formed by limited growth. As a result, the dendritic skeleton forms at the later stage of solidification. Sufficient liquid feeding is guaranteed and leads to a crack reduction.
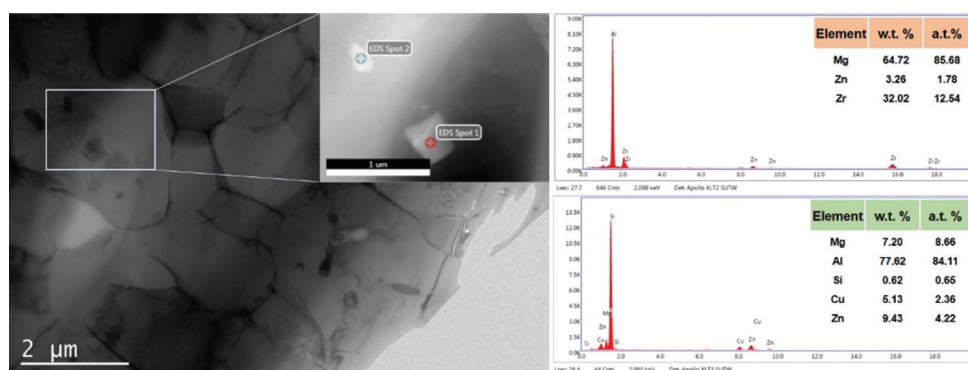

Figure 9. SEM images of samples with scanning speed 1100 mm/s and laser power 325 W. (A, C) AA7075. (B, D) 1 w.t.% Zr-modified AA7075.

Figure 10. TEM images of sample with scanning speed 1100 mm/s and laser power 325 W. The inset was taken in STEM mode, in which EDS results were measured.
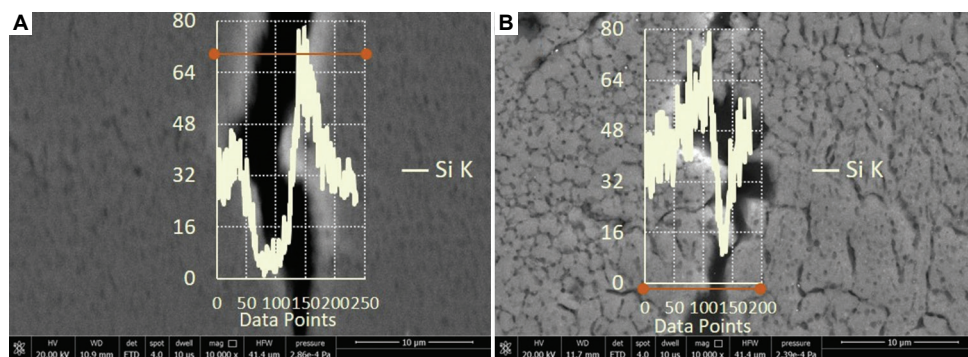

Figure 11. SEM and EDS line scans of cracks in samples with scanning speed 1100 mm/s and laser power 325 W. (A) AA7075. (B) 1 w.t.% Zr modified AA7075.

Figure 11 displays the morphology of cracks in AA7075 samples fabricated at VED 82 J/mm^3 without and with 1 w.t.% Zr addition, respectively. The crack in Figure 11A is wide and smooth-edged along the building direction, while the one in Figure 11B is curved, passing through the intergranular area. The corresponding EDS line scans display the elemental distribution of silicon near the cracks. Concentration of silicon detected near the cracks indicates that this minor element plays a significant role in increasing the susceptibility to cracking, consistent with the literature[42]. In Zr-modified parts, silicon would still segregate to the grain boundaries and may weaken the crack resistance. However, the distribution of silicon is more homogenous as fine grains result in more grain boundaries. Therefore, the effects of silicon on cracks are suppressed.

4. Conclusion

Crack-free AA7075 printed parts were obtained with elemental Zr addition. Fine equiaxed grains tend to form with VED above 76 J/mm^3. Crack-free AA7075 components were obtained with VED above 82 J/mm^3. The formation of fine equiaxed grains can be attributed to the Al$_3$Zr (the nuclei) and the limited grain growth. The formation of dendritic skeleton accompanied by sufficient liquid feeding at the later stage results in a crack reduction. Due to the deterioration of the molten pool, the viscosity by the unmelted Zr particles and the number of spherical pores tends to increase. However, with a VED above 82 J/mm^3, the porosity decreased with the ease of melt fluidity.

Conflict of interest

No potential conflict of interest was reported by the authors.

Author contributions

Conceptualization: Wenhui Yu, Zhen Xiao, Xuhui Zhang, Yongling Wu, Hongyu Zheng

Data curation: Wenhui Yu, Xuhui Zhang, Yetao Sun

Formal analysis: Wenhui Yu, Zhen Xiao, Xuhui Zhang, Yongling Wu, Hongyu Zheng

Funding acquisition: Wenhui Yu, Zhen Xiao, Hongyu Zheng

Investigation: Wenhui Yu, Xuhui Zhang, Yetao Sun

Methodology: Wenhui Yu, Zhen Xiao, Xuhui Zhang, Yetao Sun, Peng Xue, Shuai Tan, Yongling Wu, Hongyu Zheng

Project administration: Wenhui Yu, Zhen Xiao, Peng Xue, Shuai Tan, Yongling Wu, Hongyu Zheng

Resources: Xuhui Zhang, Yetao Sun

Supervision: Wenhui Yu, Zhen Xiao, Peng Xue, Shuai Tan, Yongling Wu, Hongyu Zheng

Validation: Wenhui Yu, Zhen Xiao, Yongling Wu, Hongyu Zheng

Visualization: Wenhui Yu, Xuhui Zhang

Writing – original draft: Wenhui Yu

Writing – review & editing: Wenhui Yu, Zhen Xiao, Xuhui Zhang, Yongling Wu, Hongyu Zheng

References

1. Zhang D, Qiu D, Gibson MA, *et al.*, 2019, Additive manufacturing of ultrafine-grained high-strength titanium alloys. *Nature*, 576: 91–95.

   https://doi.org/10.1038/s41586-019-1783-1

2. Wei C, Li L, 2021, Recent progress and scientific challenges in multi-material additive manufacturing via laser-based powder bed fusion. *Virtual Phys Prototyp*, 16: 347–371.

   https://doi.org/10.1080/17452759.2021.1928520

3. Sing SL, Huang S, Goh GD, *et al.*, 2021, Emerging metallic systems for additive manufacturing: *In-situ* alloying and multi-metal processing in laser powder bed fusion. *Prog Mater Sci*, 119: 100795.

   https://doi.org/10.1016/j.pmatsci.2021.100795

4. Zhou Y, Wang J, Yang Y, *et al.*, 2022, Laser additive manufacturing of zinc targeting for biomedical application. *Int J Bioprinting*, 8: 501.

   http://dx.doi.org/10.18063/ijb.v8i1.501

5. Zhang Y, Attarilar S, Wang L, *et al.*, 2021, A review on design and mechanical properties of additively manufactured NiTi implants for orthopedic applications. *Int J Bioprinting*, 7: 340–340.

   http://dx.doi.org/10.18063/ijb.v7i2.340

6. Gu D, Ma C, Dai D, *et al.*, 2021, Additively manufacturing-enabled hierarchical NiTi-based shape memory alloys with high strength and toughness. *Virtual Phys Prototyp*, 16(Suppl 1): S19–S38.

   https://doi.org/10.1080/17452759.2021.1892389

7. Yu WH, Sing SL, Chua CK, *et al.*, 2019, Particle-reinforced metal matrix nanocomposites fabricated by selective laser melting: A state of the art review. *Prog Mater Sci*, 104: 330–379.

https://doi.org/10.1016/j.pmatsci.2019.04.006

8. Xie B, Zhao MC, Xu R, *et al.*, 2020, Biodegradation, antibacterial performance, and cytocompatibility of a novel ZK30-Cu-Mn biomedical alloy produced by selective laser melting. *Int J Bioprinting*, 7: 300–300.

https://doi.org/10.18063/ijb.v7i1.300

9. Xue L, Atli KC, Zhang C, *et al.*, 2022, Laser powder bed fusion of defect-free NiTi shape memory alloy parts with superior tensile superelasticity. *Acta Mater*, 229: 117781.

https://doi.org/10.1016/j.actamat.2022.117781

10. Mukherjee T, DebRoy T, 2018, Mitigation of lack of fusion defects in powder bed fusion additive manufacturing. *J Manuf Process*, 36: 442–449.

https://doi.org/10.1016/j.jmapro.2018.10.028

11. Yonehara M, Kato C, Ikeshoji TT, *et al.*, 2021, Correlation between surface texture and internal defects in laser powder-bed fusion additive manufacturing. *Sci Rep UK*, 11: 22874.

https://doi.org/10.1038/s41598-021-02240-z

12. Moon S, Ma R, Attardo R, *et al.*, 2021, Impact of surface and pore characteristics on fatigue life of laser powder bed fusion Ti-6Al-4V alloy described by neural network models. *Sci Rep UK*, 11: 20424.

https://doi.org/10.1038/s41598-021-99959-6

13. Tang M, Pistorius PC, Beuth JL, 2017, Prediction of lack-of-fusion porosity for powder bed fusion. *Addit Manuf*, 14: 39–48.

https://doi.org/10.1016/j.addma.2016.12.001

14. Plessis AD, 2019, Effects of process parameters on porosity in laser powder bed fusion revealed by X-ray tomography. *Addit Manuf*, 30: 100871.

https://doi.org/10.1016/j.addma.2019.100871

15. Leung CL, Marussi S, Atwood RC, *et al.*, 2018, *In situ* X-ray imaging of defect and molten pool dynamics in laser additive manufacturing. *Nat Commun*, 9: 1355.

https://doi.org/10.1038/s41467-018-03734-7

16. Yu W, Sing SL, Chua CK, *et al.*, 2019, Influence of re-melting on surface roughness and porosity of AlSi10Mg parts fabricated by selective laser melting. *J Alloys Compd*, 792: 574–581.

https://doi.org/10.1016/j.jallcom.2019.04.017

17. Martin JH, Yahata BD, Hundley JM, *et al.*, 2017, 3D printing of high-strength aluminium alloys. *Nature*, 549: 365–369.

https://doi.org/10.1038/nature23894

18. Aucott L, Dong H, Mirihanage W, *et al.*, 2018, Revealing internal flow behaviour in arc welding and additive manufacturing of metals. *Nat Commun*, 9: 5414.

https://doi.org/10.1038/s41467-018-07900-9

19. Hyer H, Zhou L, Mehta A, *et al.*, 2021, Composition-dependent solidification cracking of aluminum-silicon alloys during laser powder bed fusion. *Acta Mater*, 208: 116698.

https://doi.org/10.1016/j.actamat.2021.116698

20. Hyer H, Zhou L, Mehta A, *et al.*, 2021, Effects of alloy composition and solid-state diffusion kinetics on powder bed fusion cracking susceptibility. *J Phase Equilib Diffus*, 42: 5–13.

https://doi.org/10.1007/s11669-020-00844-y

21. Riener K, Pfalz T, Funcke F, *et al.*, 2022, Processability of high-strength aluminum 6182 series alloy via laser powder bed fusion (LPBF). *Int J Adv Manuf Technol*, 119: 4963–4977.

https://doi.org/10.1007/s00170-022-08673-8

22. Tan Q, Fan Z, Tang X, *et al.*, 2021, A novel strategy to additively manufacture 7075 aluminium alloy with selective laser melting. *Mater Sci Eng A*, 821: 141638.

https://doi.org/10.1016/j.msea.2021.141638

23. Li G, Li X, Guo C, *et al.*, 2022, Investigation into the effect of energy density on densification, surface roughness and loss of alloying elements of 7075 aluminium alloy processed by laser powder bed fusion. *Opt Laser Technol*, 147: 107621.

https://doi.org/10.1016/j.optlastec.2021.107621

24. Stopyra W, Gruber K, Smolina I, *et al.*, 2020, Laser powder bed fusion of AA7075 alloy: Influence of process parameters on porosity and hot cracking. *Addit Manuf*, 35: 101270.

https://doi.org/10.1016/j.addma.2020.101270

25. Zhu Z, Ng FL, Seet HL, *et al.*, 2021, Superior mechanical properties of a selective-laser-melted AlZnMgCuScZr alloy enabled by a tunable hierarchical microstructure and dual-nanoprecipitation. *Mater Today*,

https://doi.org/10.1016/j.mattod.2021.11.019

26. Lei Z, Bi J, Chen Y, *et al.*, 2019, Effect of energy density on formability, microstructure and micro-hardness of selective laser melted Sc- and Zr- modified 7075 aluminum alloy. *Powder Technol*, 356: 594–606.

https://doi.org/10.1016/j.powtec.2019.08.082

27. Shrivastava V, Singh P, Gupta GK, *et al.*, 2021, Synergistic effect of heat treatment and reinforcement content on the microstructure and corrosion behavior of Al-7075 alloy based nanocomposites. *J Alloys Compd*, 857: 157590.

https://doi.org/10.1016/j.jallcom.2020.157590

28. Liu L, Jiang JT, Cui XY, *et al.*, 2022, Correlation between precipitates evolution and mechanical properties of Al-Sc-Zr

alloy with Er additions. *J Mater Sci Technol*, 99: 61–72.

https://doi.org/10.1016/j.jmst.2021.05.031

29. Qi Y, Hu Z, Zhang H, *et al.*, 2021, High strength Al-Li alloy development for laser powder bed fusion. *Addit Manuf*, 47: 102249.

https://doi.org/10.1016/j.addma.2021.102249

30. Otani Y, Sasaki S, 2020, Effects of the addition of silicon to 7075 aluminum alloy on microstructure, mechanical properties, and selective laser melting processability. *Mater Sci Eng A*, 777: 139079.

https://doi.org/10.1016/j.msea.2020.139079

31. Glerum JA, Kenel C, Sun T, *et al.*, 2020, Synthesis of precipitation-strengthened Al-Sc, Al-Zr and Al-Sc-Zr alloys via selective laser melting of elemental powder blends. *Addit Manuf*, 36: 101461.

https://doi.org/10.1016/j.addma.2020.101461

32. Zhu Y, Zhao Y, Chen B, 2022, A study on Sc- and Zr-modified Al-Mg alloys processed by selective laser melting. *Mater Sci Eng A*, 833: 142516.

https://doi.org/10.1016/j.msea.2021.142516

33. Mehta A, Zhou L, Huynh T, *et al.*, 2021, Additive manufacturing and mechanical properties of the dense and crack free Zr-modified aluminum alloy 6061 fabricated by the laser-powder bed fusion. *Addit Manuf*, 41: 101966.

https://doi.org/10.1016/j.addma.2021.101966

34. Hyer H, Zhou L, Park S, *et al.*, 2022, Elimination of extraordinarily high cracking susceptibility of aluminum alloy fabricated by laser powder bed fusion. *J Mater Sci Technol*, 103: 50–58.

https://doi.org/10.1016/j.jmst.2021.06.023

35. Li P, Li R, Yang H, *et al.*, 2021, Selective laser melting of Al-3.48Cu-2.03Si-0.48Sc-0.28Zr alloy: Microstructure evolution, properties and metallurgical defects. *Intermetallics*, 129: 107008.

36. Zhang X, Xiao Z, Yu W, *et al.*, 2022, Influence of erbium addition on the defects of selective laser-melted 7075 aluminium alloy. *Virtual Phys Prototyp*, 17: 406-418.
https://doi.org/10.1080/17452759.2021.1990358

37. Martin A, Vilanova M, Gil E, *et al.*, 2022, Influence of the Zr content on the processability of a high strength Al-Zn-Mg-Cu-Zr alloy by laser powder bed fusion. *Mater Charact*, 183: 111650.
https://doi.org/10.1016/j.matchar.2021.111650

38. Hojjatzadeh SMH, Parab ND, Guo Q, *et al.*, 2020, Direct observation of pore formation mechanisms during LPBF additive manufacturing process and high energy density laser welding. *Int J Mach Tools Manuf*, 153: 103555. https://doi.org/10.1016/j.ijmachtools.2020.103555

39. Gu D, Yuan P, 2015, Thermal evolution behavior and fluid dynamics during laser additive manufacturing of Al-based nanocomposites: Underlying role of reinforcement weight fraction. *J Appl Phys*, 118: 233109.
https://doi.org/10.1063/1.4937905

40. Gu D, Ma C, Xia M, *et al.*, 2017, A Multiscale understanding of the thermodynamic and kinetic mechanisms of laser additive manufacturing. *Engineering PRC*, 3: 675-684.
https://doi.org/10.1016/J.ENG.2017.05.011

41. Khvan AV, Eskin DG, Starodub KF, *et al.*, 2018, New insights into solidification and phase equilibria in the Al-Al$_3$Zr system: Theoretical and experimental investigations. *J Alloys Compd*, 743: 626–638.
https://doi.org/10.1016/j.jallcom.2018.02.023

42. Uddin SZ, Murr LE, Terrazas CA, *et al.*, 2018, Processing and characterization of crack-free aluminum 6061 using high-temperature heating in laser powder bed fusion additive manufacturing. *Addit Manuf*, 22: 405–415. https://doi.org/10.1016/j.addma.2018.05.047